Progress In Electromagnetics Research C, Vol. 167, 196–204, 2026 PIER C

(Received 28 January 2026, Accepted 21 February 2026, Scheduled 21 March 2026)

Compact Tri-Band Semi-Elliptical Monopole Antenna with Improved Filtering Characteristics for 5G, V2X, WLAN, and Wi-Fi 6E Applications

Sheetal Mete[1,*], Jagadish Jadhav[2], Brijesh Iyer[1], Anjali Rochkari[3], and Sanjay L. Nalbalwar[1]

[1]*Dr. Babasaheb Ambedkar Technological University, Lonere, Raigad, India*
[2]*R. C. Patel Institute of Technology, Shirpur, Dhule, Maharashtra, India*
[3]*Terna Engineering College, Navi-Mumbai, India*

ABSTRACT: In this paper, an elliptical monopole antenna is modified and loaded with stubs and slots to improve the filtering characteristics over tri-band operation. As the surface current is concentrated at the periphery of the monopole and decreases away from the feed, a slotted elliptical monopole is designed and sliced from the top. A rectangular strip is added at the top and center to create two symmetrical loops. A slot in each loop at a different position causes the antenna to operate over dual/tri-bands. A rectangular stub is added to the feed-line to improve the band-stop/filtering characteristics. The parameters of the structure are optimized to obtain $S_{11} \leq -10\,\text{dB}$ over 3.22–3.64 GHz, 5.53–6.03 GHz and 6.71–7.14 GHz for 5G, V2X, WLAN, and Wi-Fi 6E applications. The three bands can be tuned independently. The compact $0.171\lambda_0 \times 0.184\lambda_0$ antenna, fabricated on a 1.6 mm FR4 substrate (λ_0 is the free-space wavelength at 3.22 GHz), offers maximum S_{11} of $-0.9\,\text{dB}$ and $-4.9\,\text{dB}$, respectively, between the lower and middle bands and middle and upper bands. Minimum S_{11} of $-55\,\text{dB}$, $-25\,\text{dB}$, and $-27\,\text{dB}$ are obtained over the lower, middle, and upper bands, respectively. The measured results validate the simulation ones.

1. INTRODUCTION

Technological advancements and their proliferation have increased data consumption, providing connectivity for work from remote places. There has been tremendous growth in mobile networks and wireless devices networks, which has led to increased data consumption. The continuous evolution of wireless technology has paved the way for fifth-generation (5G) technology. Researchers and technocrats are on their toes to not only increase the functionality of the product but also provide better performance at a lower cost. These factors, along with their small size, are the primary drivers of technological development. 5G technology offers a solution to societal challenges and competitive economic advantages as it provides continuous, reliable, and high-speed connectivity with low latency. The antenna plays a key role in wireless systems. The functionality, performance, cost, and size of wireless systems rely heavily on the design of the antennas. Researchers are always in search of novel compact antennas with low cost, improved performance, and increased functionality.

In a monopole antenna, several modes, each with a broad bandwidth (BW), are excited and electromagnetically coupled to provide an ultra-wideband (UWB) response. The dimensions and shape of the radiator and the ground plane determine the BW of the monopole antenna [1, 2]. An elliptical ring monopole antenna operating over 3.6–15.46 GHz [3] and a metallic dual-concentric circular ring monopole antenna operating over 3.03–11.75 GHz [4] are designed, and characteristic modes are analysed in [3, 4]. A super wideband (1.613–26.357 GHz) monopole antenna with elliptical slots is reported in [5]. A slotted antenna is designed and loaded with a rectangular ring to offer circular polarization over 4.47–6.89 GHz [6]. However, UWB monopole antennas interfere with other wireless devices operating within narrow bands of the UWB spectrum. To mitigate this interference, antennas with single or multiple band notches have been designed [7–9]. Filtering antenna [10, 11] and filters are designed for integration with antennas [12].

A multiband antenna offers increased functionality and better performance than several narrow-band antennas. Multiple narrow-band antennas require more space and add complexity and weight to a wireless device, whereas a wideband antenna operating over several bands may cause a poor signal-to-noise ratio. A monopole antenna with multiple branches yields a multiband antenna, because each branch resonates at a frequency depending on its length, and its width determines the bandwidth. Compact multiband monopole antennas are designed with various branch shapes [13–16]. Tri-band antennas of modified F-shaped [13], two connected curved C-shaped [14], slotted S-shaped [15], and hybrid-shaped [16] ones have been reported. In another technique, stubs, slits, and slots are etched in a radiating patch and a ground plane to design multiband antennas. A dual-band metallic slotted-loop antenna is loaded with two T-stubs in [17]. Tri-band and dual-band antennas are designed using multiple slots/slits and stubs for Blue-

---

[*] Corresponding author: Sheetal Mete (shital.mete@gmail.com).

doi:10.2528/PIERC26012803 Published by THE ELECTROMAGNETIC ACADEMY

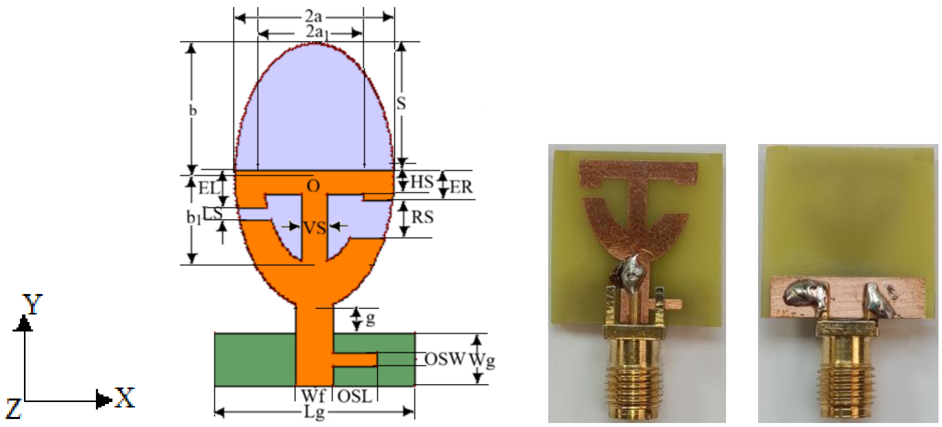

FIGURE 1. Geometry and photographs (bottom and top views) of the fabricated antenna.

tooth, Wi-Max, and WLAN applications in [18, 19]. A dual-band antenna is designed using slots in a rectangular patch for 5G and WLAN applications [20]. Parasitic elements and shorting posts/vias are used to design a compact dual-band antenna [21], while the frequency coverage of a dual-band antenna is maximized by using a metallic wire discone with printed meander-line dipoles in [22].

Multiband reconfigurable antennas are designed to enhance the functionality and utility of antennas using PIN diodes in slots incorporated in the radiating patch and ground plane [23, 24]. Multiband fractal antennas are reported in [25, 26]. Metamaterial-based multiband antennas have been designed [27, 28]. An octagonal ring monopole antenna using a split-ring resonator (SRR) and complementary SRR (CSRR) offers penta-band operation [27]. The CSRR is etched in a rectangular radiator to design a dual-band antenna in [28]. A dual-band antenna using a negative metamaterial is reported in [29]; however, the reported antennas are complex in design and larger in dimensions than our proposed antenna.

In this paper, a novel compact tri-band antenna is proposed for 5G (3.3–3.6 GHz), V2X and WLAN (5.725–5.925 GHz), and Wi-Fi 6E (6.875–7.125 GHz) applications. The antenna is miniaturized by etching the conducting area with a low surface current density. A slotted elliptical antenna is sliced from the top, and a T-strip is added. A slot is etched in each of the two loops to obtain tri-band operation. An open stub is added to the feed line to improve the matching and stopband characteristics. $S_{11} \leq -10$ dB is obtained over 3.22–3.64 GHz, 5.53–6.03 GHz, and 6.71–7.14 GHz. The proposed structure (PS) offers minimum S_{11} of -55 dB, -25 dB, and -27 dB over the lower, middle, and upper bands, respectively, and maximum S_{11} of -0.9 dB and -4.9 dB, respectively, between the lower and middle bands and middle and upper bands. In this regard, PS is superior to other reported antennas. The three bands of the PS can be tuned independently. The low-cost compact structure is simple to design and offers stable omnidirectional radiation characteristics.

2. DESIGN THEORY AND ANTENNA GEOMETRY

A multiband antenna can be designed from a UWB antenna by reducing the electromagnetic coupling (EMC) between fundamental and higher-order modes. The shape and size of the monopole and ground plane, and the spacing between the two determine the number of excited modes and the EMC between them. The width of the circular monopole antenna (CMA) is decreased, and the gap/spacing between the ground-plane edge and radiator is increased to reduce the number of excited modes and the EMC between them, resulting in an elliptical monopole antenna (EMA).

In EMA, a slot can be etched at the center because the surface current is mainly concentrated at the periphery. In a slotted EMA (SEMA), as the surface current density at the periphery (conducting area) increases owing to etching, the resonant frequencies of the fundamental and higher-order modes decrease marginally due to an increase in the effective current path length. The surface current density also decreases from the area near the feed-line to the area away from the feed-line. Therefore, a portion of the SEMA from the top is sliced. In sliced SEMA, the resonant frequencies increase slightly due to a decrease in the effective current path length.

A T-shaped strip is added to the sliced SEMA to form two loops. Slots are etched in the elliptical-shaped side of the two loops to increase the capacitive impedance, decrease the resonant frequency, and miniaturize the antenna. The position and width of the slots in the ellipse-shaped side affect impedance-matching and resonant frequency. An open stub is added to the feed line to enhance the stopband characteristics and improve impedance matching. Fig. 1 displays the geometry and photograph of the semi-elliptical triband antennas with slots and stubs. Table 1 lists the dimensions of the optimum parameters of the proposed antenna.

TABLE 1. Optimized parameters' dimensions in mm.

L_g	W_g	W_f	G	a	b	a_1	b_1	S
16	4.2	3	2.0	6.3	10.5	4.0	7.0	10.0
HS	VS	EL	ER	LS	RS	OSL	OSW	
2.0	2.0	3.0	2.5	1.0	3.0	3.5	1.0	

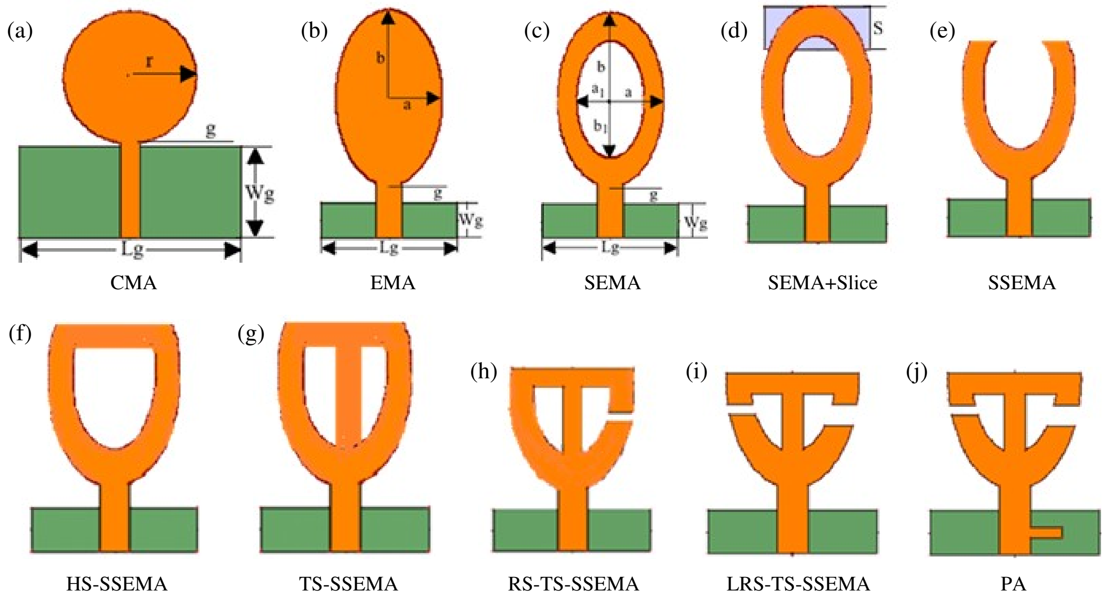

FIGURE 2. Development stages of the proposed antenna.

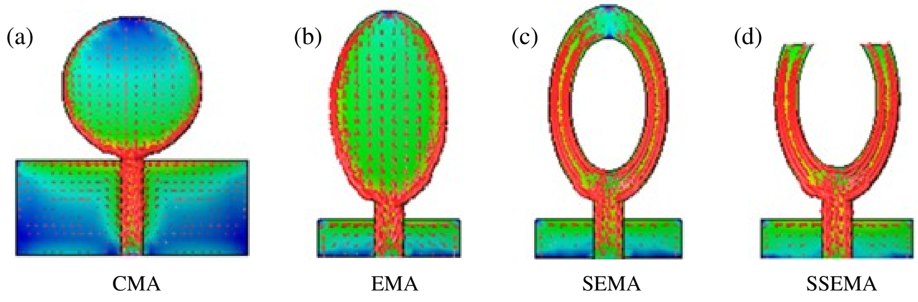

FIGURE 3. Surface current density.

2.1. Development Stages of Proposed Antenna

The step-by-step development of the antenna is illustrated in Fig. 2. The antenna is designed from a circular monopole antenna (CMA). A CMA with radius $r = 10.2\,\text{mm}$ is designed on a 1.6 mm FR4 substrate (Fig. 2(a)). The ground plane dimensions are $L_g = 34\,\text{mm}$ and $W_g = 14\,\text{mm}$. The gap 'g' between the ground plane and monopole radiator is 0.5 mm. The lowest operating frequency corresponding to $S_{11} = -10\,\text{dB}$ is given by Equation (1) [1]

$$f_L = 72/(k \cdot (2.25r + g)) \tag{1}$$

$k = 1.15$ depends on the substrate material and its thickness [30]. The calculated $f_L = 2.67\,\text{GHz}$ is close to the simulated $f_L = 2.61\,\text{GHz}$. To reduce the number of modes and the EMC between them, the width of the monopole and ground-plane dimensions are decreased, and the gap 'g' is increased. Therefore, an EMA ($a = 6.3\,\text{mm}$ and $b = 10.5\,\text{mm}$) is designed on a $16.2\,\text{mm} \times 4.2\,\text{mm}$ ground-plane with gap 'g' $= 2\,\text{mm}$ (Fig. 2(b)).

Since the surface current flows along the periphery of the EMA (Fig. 3), an elliptical slot $(a_1 \times b_1)$ of $4\,\text{mm} \times 7\,\text{mm}$ is etched from the EMA, resulting in a slotted EMA (SEMA) (Fig. 2(c)). S_{11} and the impedance variation plots for CMA, EMA, and SEMA are shown in Fig. 4. The number of modes and EMC are maximum in CMA and minimum in SEMA, as evident from the S_{11} plot. The loop size on the impedance variation plot is the smallest in the case of CMA, the strongest EMC, and the largest in SEMA, which represents the weakest EMC. An increase in loop size indicates a decrease in the EMC.

The effect of the elliptical slot dimensions $(a_1 \times b_1)$ in the SEMA is analyzed. As the slot dimensions are increased, the surface current density on the remaining conducting part increases; therefore, the resonant frequencies of both bands decrease. S_{11} and the impedance variation plots for different slots are shown in Fig. 5. As the slot size increases, the capacitive impedance increases, and the impedance variation curve shifts downward.

In SEMA, the surface current density is maximum near the ground-plane edge and minimum at the top (away from the ground-plane edge) (Fig. 3). Therefore, a portion of the SEMA from the top is sliced. SEMA with sliced portion and sliced SEMA (SSEMA) are shown in Figs. 2(d) and 2(e), respectively. The effect of the amount of sliced portion 'S' on S_{11} in the SEMA is analyzed. The resonant frequencies of the fundamental and higher-order modes increase slightly because of a decrease in the effective current-path length as 'S' increases. The

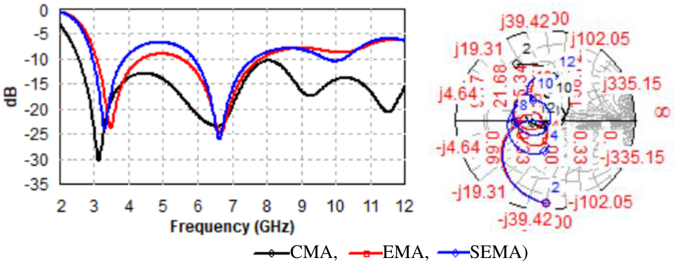

FIGURE 4. S_{11} and impedance variation.

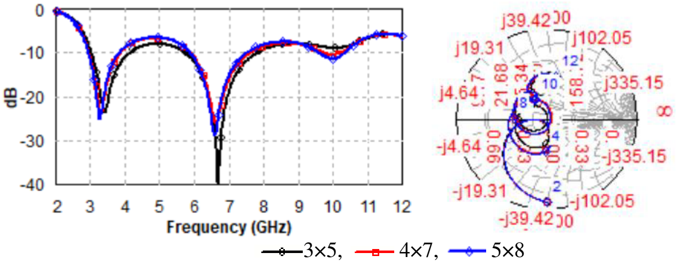

FIGURE 5. S_{11} and impedance variation for different slots.

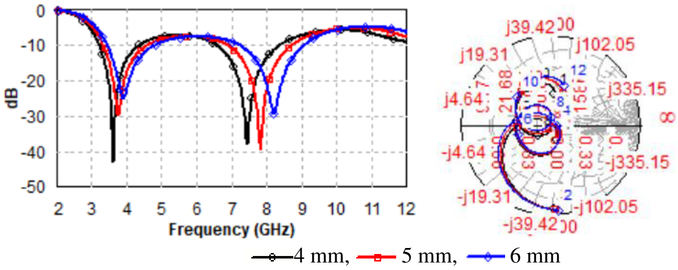

FIGURE 6. S_{11} and impedance variation for different slicing 'S'.

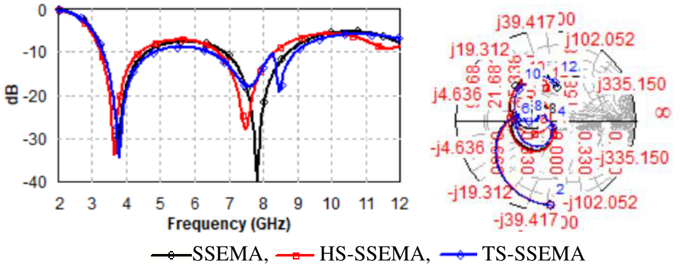

FIGURE 7. S_{11} and impedance variation.

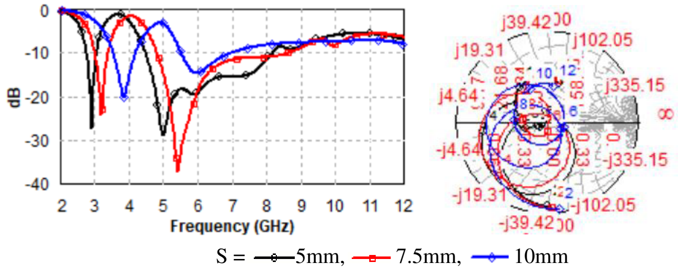

FIGURE 8. S_{11} and impedance variation of RS-TS-SSEMA.

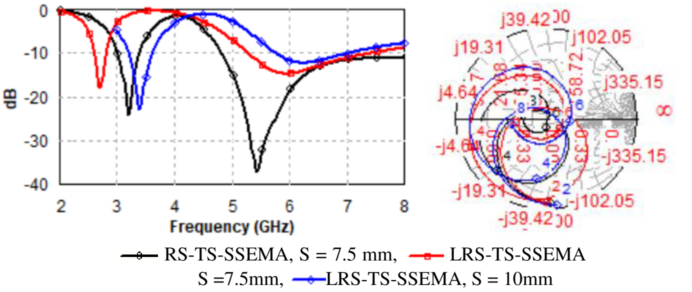

FIGURE 9. S_{11} and impedance variation.

impedance matching also degrades with an increase of 'S'. S_{11} and the impedance variation plots for different 'S' are shown in Fig. 6. As the spacing between the two elliptical arms increases with an increase in 'S', the capacitive impedance decreases, and the impedance variation curve shifts upward with an increase in 'S'.

The open-ended SSEMA ($S = 5$ mm) is closed using a 2 mm horizontal strip, termed 'HS-SSEMA' (Fig. 2(f)). Adding the strip increases the inductive impedance and lowers the resonant frequencies of the lower and upper bands. A 2 mm vertical strip is added to this closed sliced SEMA, resulting in the addition of a T-shaped strip to the open-ended sliced SEMA, termed 'TS-SSEMA' (Fig. 2(g)). The vertical strip increases the EMC between the two conducting loops. As a result, three loops are observed in the impedance variation plot, and the BW of the upper band increases significantly. The impedance variation and S_{11} plots are shown in Fig. 7.

A slot of 1 mm is etched at 7.5 mm from the bottom point of the ellipse in the right elliptical arm of the TS-SSESMA. This structure is termed as RS-TS-SSESMA (Fig. 2(h)). It increases the capacitive impedance of the structure; therefore, the resonant frequency decreases. $S_{11} < -10$ dB is obtained over 2.78–3.05 GHz and 4.49–8.13 GHz. As a result, the dimensions of the structure are decreased. The SEMA is sliced by 7.5 mm and then by 10 mm from the top, and a T-strip is added. Then, a slot of 1 mm is etched at 7.5 mm from the bottom point of the ellipse. S_{11} and impedance plots of the structures are shown in Fig. 8. As 'S' increases and the size of TS-SSEMA decreases, the capacitive impedance of the structure decreases, and the impedance variation curve shifts upward. The resonant frequencies increase with a decrease in the size of TS-SSEMA. However, impedance matching and S_{11} degrade with a decrease in the size of the TS-SSEMA structure.

A slot of 1 mm is now etched at 7.5 mm from the bottom point of the ellipse in the left elliptical side of RS-TS-SSEMA, referred to as LRS-TS-SSEMA structure, with $S = 7.5$ mm and 10 mm (Fig. 2(i)). S_{11} and the impedance variation plots of RS-TS-SSEMA ($S = 7.5$ mm), LRS-TS-SSEMA ($S = 7.5$ mm), and LRS-TS-SSEMA ($S = 10$ mm) structures are shown in Fig. 9. As the capacitive impedance of the structure increases when the slot is etched in the left elliptical side, the resonant frequency of the lower-band decreases. The impedance variation loop of LRS-TS-SSEMA ($S = 7.5$ mm) shifts left and downward in comparison to RS-TS-SSEMA ($S = 7.5$ mm), and the

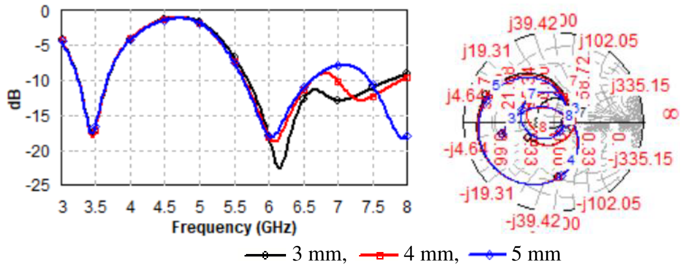

FIGURE 10. S_{11} and impedance variation for different right-slot (RS) widths in LRS-TS-SSEMA ($LS = 1\,\text{mm}$).

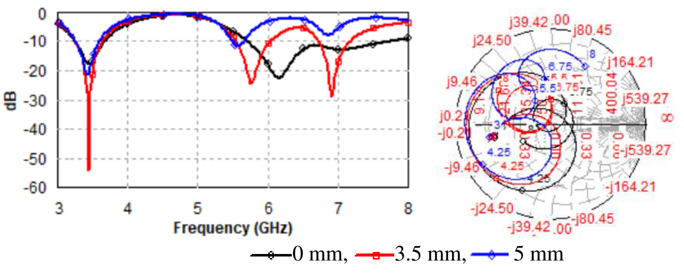

FIGURE 11. S_{11} and impedance variation with different OSL.

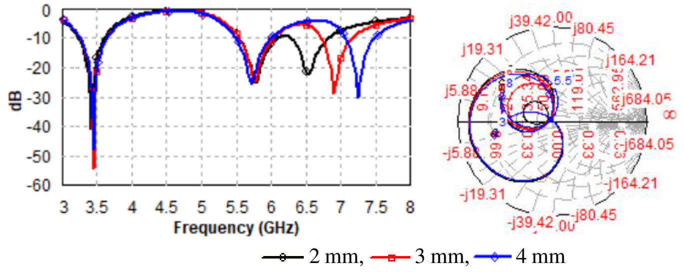

FIGURE 12. S_{11} and impedance variation of PS with different RS.

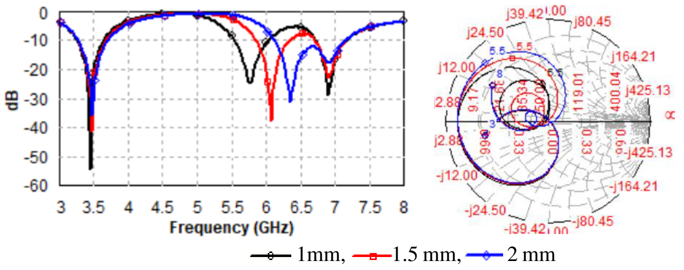

FIGURE 13. S_{11} and impedance variation of PS with different LS.

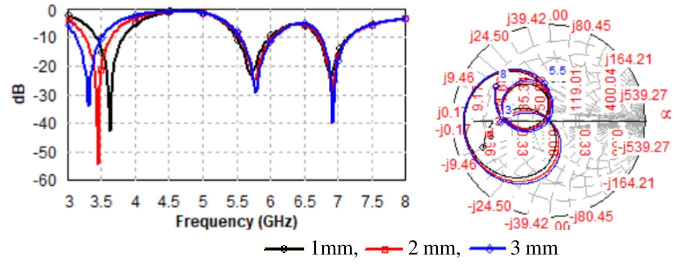

FIGURE 14. S_{11} and impedance variation of PS with different HS.

loop size also increases, indicating a reduction in the EMC. However, S_{11} degrades significantly over the upper band. The resonant frequency increases with a decrease in the dimensions of the structure ($S = 10\,\text{mm}$). The inductive impedance increases, and the impedance variation plot shifts upward. The LRS-TS-SSEMA ($S = 10\,\text{mm}$) structure offers $S_{11} < -10\,\text{dB}$ over the frequency ranges of 3.2–3.61 GHz and 5.75–7.01 GHz. However, S_{11} is unsatisfactory and requires improvement.

The effect of the width of the right slot in the LRS-TS-SSEMA structure with $S = 10\,\text{mm}$ is analyzed. The right slot width is varied, whereas the left slot width is fixed at 1 mm. As the slot width is increased, there is no significant effect on the lower band; however, the loop size on the impedance variation plot increases, indicating a reduction in the EMC. S_{11} degrades over the upper-band. S_{11}, and the impedance plots for different right-slot (RS) widths in LRS-TS-SSEMA are shown in Fig. 10. Similar results are obtained when the left slot width is varied in the LRS-TS-SSEMA structure with $S = 10\,\text{mm}$, whereas the right slot width is fixed at 1 mm.

2.2. Proposed Antenna and Major Parameters

An open stub ($OSL = 3.5\,\text{mm} \times OSW = 1.0\,\text{mm}$) is added to the feed line of the LRS-TS-SSEMA, referred to as the OS-LRS_TS_SSEMA/proposed structure ($LS = 1\,\text{mm}$, $RS = 3\,\text{mm}$, $S = 10\,\text{mm}$) to improve the stopband characteristics and impedance matching (Fig. 2(j)). An open stub less than a quarter wavelength acts as a frequency-dependent shunt capacitor and thus helps in improving impedance matching and band-stop characteristics. Since the electrical length of the stub increases with frequency, the capacitance value of the stub and its effect on the impedance of the structure vary with frequency. The effect of the stub is analyzed. The structure with no stub has poor impedance matching and a wide upper band. The structure with an open stub of $OSL = 5\,\text{mm}$ also suffers from poor impedance matching. The impedance matching and stopband filtering characteristics improve significantly with an open stub of $OSL = 3.5\,\text{mm}$. S_{11} and the impedance variation plots of PS for different stub lengths 'OSL' are shown in Fig. 11. The impedance variation curve of $OSL = 3.5\,\text{mm}$ is closer to the center of the Smith chart than impedance curves with no stub ($OSL = 0\,\text{mm}$) and $OSL = 5\,\text{mm}$ over all three bands.

The width of the right slot is also varied in PS. As the right slot width increases, the loop size on the impedance variation curve also increases, indicating a decrease in the EMC. The impedance variation curve passes near the $50\,\Omega$ point on three separate occasions, enabling the possibility of operation across three distinct frequency bands. $RS = 2\,\text{mm}$ offers a wide upper band due to EMC. However, the structure operates over three distinct bands as RS is increased to 3 or 4 mm. The increase in the right slot width has a negligible effect on the lower-band and little effect on the middle-band; however, the resonant frequency of the upper band increases. S_{11} and the impedance variation plots of the proposed structure (PS) for different RS are shown in Fig. 12.

In PS with $RS = 3\,\text{mm}$, the effect of the width of the left slot is analyzed. The width of the left slot affects the resonant frequency of the middle band. The width of the left slot has a

TABLE 2. Values of elements of the equivalent circuit of the proposed antenna.

Parameters	Lower band ($i=1$)	Middle band ($i=2$)	Upper band ($i=3$)
Resonant frequency (fo_i) GHz	3.445	5.767	6.902
Band width (BW_i) GHz	0.387	0.492	0.448
Quality Factor (Q_i)	8.902	11.722	15.406
Resistance (R_i) Ω	50.07	45.17	47.31
Inductance (L_i) nH	20.59	14.61	16.81
Capacitance (C_i) pf	0.104	0.052	0.032

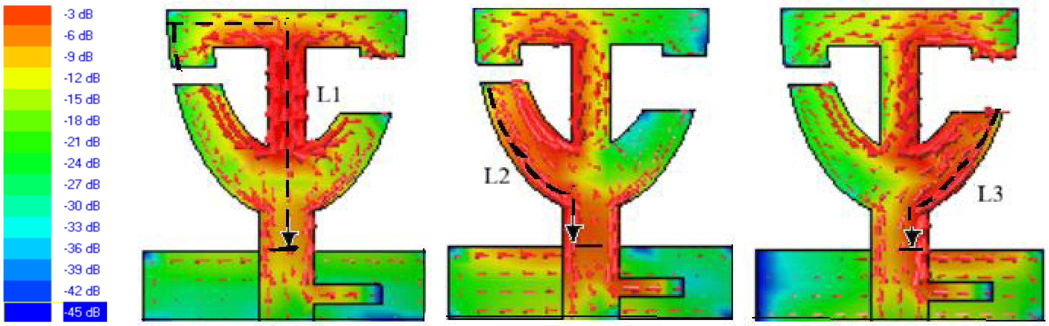

3.45 GHz 5.75 GHz 6.9 GHz

FIGURE 15. Scalar and vector surface current distributions of PS.

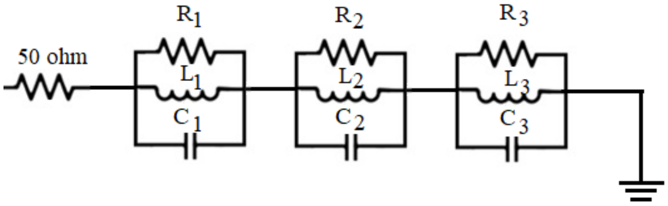

FIGURE 16. Equivalent circuit of proposed tri-band antenna [31].

negligible effect on the resonant frequencies of the other bands. However, as the left slot width increases, the loop size on the impedance variation curve decreases, indicating a decrease in the EMC, resulting in a wideband upper band for $LS = 2\,\mathrm{mm}$. S_{11} and the impedance variation plots of PS for different LS are shown in Fig. 13. The analysis illustrates that the middle and upper bands can be controlled independently by LS and RS, respectively.

The effect of T-strip width 'HS' of the proposed structure is also analyzed. As 'HS' increases, the resonant frequency of the lower band decreases with little effect on the other two bands. The loop size of the impedance variation curve increases slightly with an increase in 'HS', indicating a decrease in the EMC. S_{11} and the impedance variation plot of the PS for different HS are shown in Fig. 14. The three bands can be independently controlled and tuned by varying the dimensions of HS, LS, and RS. The antenna parameters are optimized to operate over 5G, WLAN, V2X, and Wi-Fi 6E bands. $S_{11} \leq -10\,\mathrm{dB}$ over 3.22–3.64 GHz, 5.53–6.03 GHz and 6.71–7.14 GHz is obtained.

The surface current density at the resonant frequencies of the three bands is shown in Fig. 15. At 3.45 GHz, the surface current is concentrated along the T-strip. Therefore, length L_1 determines the resonant frequency of the lower band. At 5.75 GHz, the intense surface current is along the left elliptical side. Therefore, length L_2 determines the resonant frequency of the middle band. At 6.9 GHz, the intense surface current is along the right elliptical side. Therefore, length L_3 determines the resonant frequency of the upper band.

2.3. Equivalent Circuit

The equivalent circuit of the tri-band antenna is shown in Fig. 16. Three parallel resonating circuits represent the three bands. The elements R_1, L_1, and C_1, R_2, L_2, and C_2 and R_3, L_3, and C_3 represent the lower band, middle band, and upper band, respectively. The values of these elements can be calculated using Equations (2)–(5) [31].

$$\omega_i = 2\pi fo_i \tag{2}$$

$$fo_i = 1/2\pi\sqrt{L_i C_i} \tag{3}$$

$$Q_i = fo_i/BW_i = \omega_i L_i/R_i \tag{4}$$

$$C_i = \varepsilon_0 \varepsilon_r Si/h \tag{5}$$

Here fo_i, ω_i, Q_i, and BW_i are resonant frequency, angular frequency, quality factor, and bandwidth of 'i' band respectively, whereas R_i, L_i, and C_i are the resistance, inductance, and capacitance of 'i' band, respectively. ε_0, ε_r, and h represent the permittivity of free-space, dielectric constant, and thickness of the substrate, respectively. Si is the surface area of that part of the antenna that radiates over a band. The values of elements of the equivalent circuit are calculated using Equations (2)–(5) [31] and listed in Table 2.

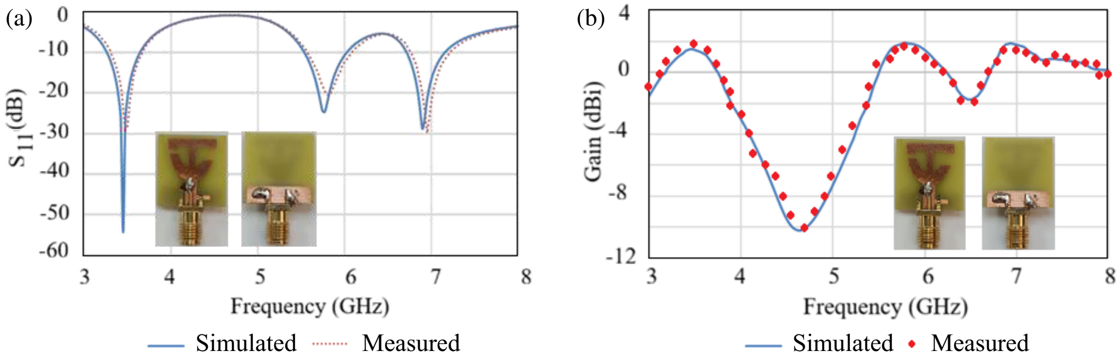

FIGURE 17. (a) S_{11}. (b) Gain.

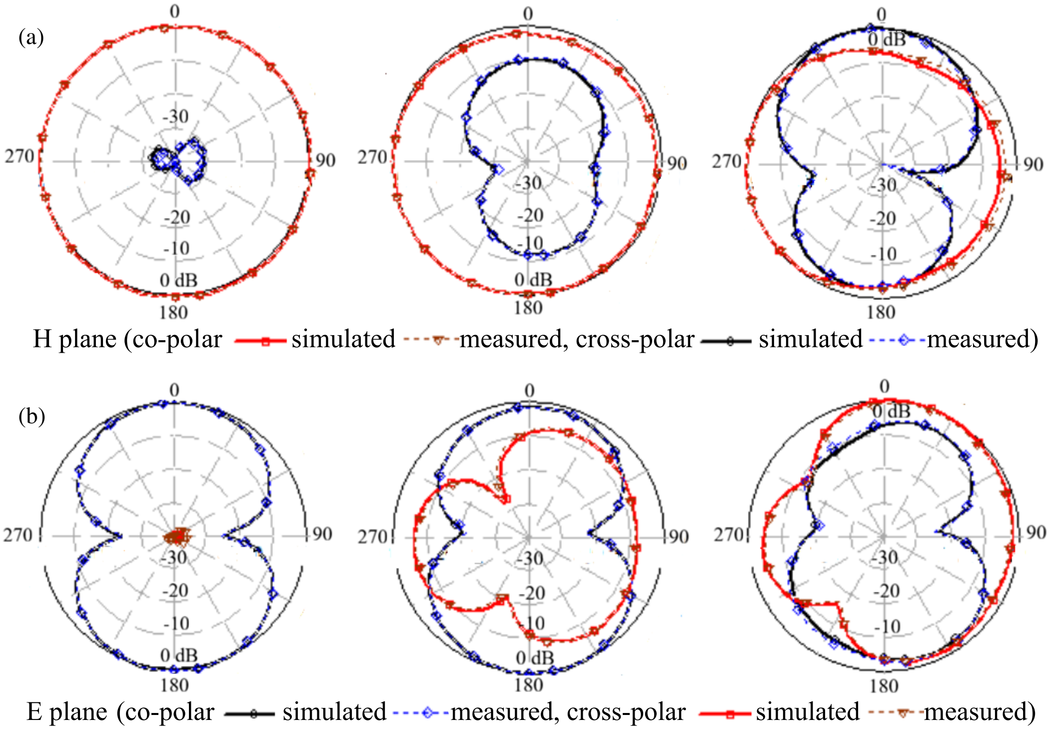

3.5 GHz 5.75 GHz 6.9 GHz

FIGURE 18. Radiation patterns of tri-band antenna.

3. FABRICATION AND MEASURED RESULTS

The antenna is fabricated (Fig. 1). The S_{11} measurement is performed in an anechoic chamber using a 9916 A Agilent-make VNA. The instruments, along with the adaptors/connectors and cables, are calibrated to mitigate the testing errors. A standard horn antenna, 9916 A VNA, and a spectrum analyzer in an anechoic chamber are used to measure the gain and radiation patterns of the prototype antenna in the far-field region. Simulated and measured S_{11} and gains are shown in Fig. 17. The measured results validate the simulated ones. The gain is almost constant, and the variation is < 1.5 dB over three bands. The measured radiation patterns at 3.45 GHz, 5.75 GHz, and 6.9 GHz are shown in Fig. 18. The radiation patterns are nearly omnidirectional in the H-plane and figure-of-eight in the E-plane. However, as the frequency increases, the radiation pattern deviates and becomes more directional. At 5.75 GHz and 6.9 GHz, the elliptical sides radiate, while the T-strip acts as a reflector and distorts the radiation patterns. As the frequency increases, the electrical thickness of the substrate increases, and therefore, cross-polarization increases due to an increase in the surface waves. The discrepancy between measured and simulated results can be attributed to fabrication errors, connector loading, substrate material, and improper alignment of the test antenna.

4. COMPARISON WITH RECENTLY REPORTED ANTENNAS

The designed antenna structure (PS) is compared with recently reported multiband antenna structures in Table 3 with respect to the techniques used, number of bands, and antenna size. The designed antenna is compact and smaller than recently re-

TABLE 3. Comparison of the designed antenna with the recent reported multiband antennas.

Ref.	Technique used	Antenna Size (mm^2)	Bands (GHz)/%BW	Electrical Size ($\lambda_o \times \lambda_o$)	Gain (dBi)
[13]	Modified F-shaped multiple branches — tri-band	40×28	2.2–2.6, 5.3–6.8, 8.7–9.5, 16.7, 24.8, 8.8	$0.293 \times 0.205 = 0.0606\lambda_o^2$	1.45, 3.53, 4.98
[14]	Modified dual C-shaped branches — tri-band	24×28	2.34–2.55, 3.39–3.69, 5.5–6.0, 8.6, 8.5, 8.7	$0.187 \times 0.2184 = 0.0408\lambda_o^2$	2.3, 2.6, 3.7
[15]	S-shaped with a slot — tri-band	13×12.8	7.44–7.695, 8.86–9.22, 26.79–29.43, 3.4, 4.0, 9.4	$0.2 \times 0.317 = 0.1021\lambda_o^2$	3.96, 3.05, 5.86
[16]	Multiple-branches, two meander line shaped, I-shaped and L-shaped — quad band	32×21	1.7–1.96, 2.26–2.47, 3.1–3.7, 5–5.65, 14.2, 8.9, 17.6, 12.2	$0.1813 \times 0.119 = 0.0216\lambda_o^2$	1.5, 1.75, 2.5, 3.7
[17]	Three loop-slots each loaded with T-shaped stub – dual band	35×37	2.15–2.65, 4.85–5.92, 20.8, 19.9	$0.251 \times 0.265 = 0.0665\lambda_o^2$	2.39, 4.51
[18]	Multiple slots and slits on the ground plane — tri-band	50×50	1.6–2.8, 3.38–3.6, 5.55–6.36, 54.5, 6.3, 13.6	$0.2667 \times 0.2667 = 0.07113\lambda_o^2$	3.48, 3.10, 4.93
[19]	Multiple slots and stubs on the ground plane — tri-band	43×33	2.28–3.1, 3.52–4.1, 5.05–6.0, 30.5, 15.2, 17.2	$0.3268 \times 0.2508 = 0.08196\lambda_o^2$	5.5, 0.0, 5.6
[20]	Slots in a rectangular patch — dual-band	14×17	3.3–3.6, 5.5–5.9, 8.7, 7.0	$0.154 \times 0.187 = 0.0283\lambda o^2$	1.0, 3.5
[24]	Two branches of different lengths — dual-band	17×22	4.36–4.70, 5.60–5.96, 7.7, 6.2	$0.25 \times 0.32 = 0.08\lambda_o^2$	3.3, 3.0
[27]	Octagonal ring with multiple slots and metamaterial cells — penta-band	33×22	3.19–3.96, 4.65–5.33, 6.78–7.54, 10.0–14.29 15.74–19.98, 21.5, 11.7, 10.6, 35.3, 23.74	$0.3509 \times 0.2339 = 0.08207\lambda_o^2$	2.51, 1.52, 1.51, 2.48, 3.58
[28]	CSRR etched in a rectangular patch — Dual band	34×20	1.78–1.90, 3.45–6.58, 6.5, 62.4	$0.2017 \times 0.1187 = 0.0239$	2.3, 2.3
PS	Slotted and sliced semi-elliptical-shaped monopole with T-strip, slots and stub-tri-band	16×17.2	3.22–3.64, 5.53–6.03, 6.71–7.14, 12.2, 8.7, 6.2	$0.171 \times 0.184 = 0.03146\lambda_o^2$	1.8, 2.0, 1.9

ported antennas, except for [16, 20, 28]. The antenna in [16] is a quad-band antenna designed using multiple branches of different shapes on a slotted tapered trapezoidal ground plane; therefore, it is difficult to design. Refs. [20] and [28] are dual-band antennas. The CSRR is engraved in a rectangular patch in [28], whereas slots are etched in a rectangular ring in [20]. The PS is a triband antenna and offers much better impedance matching (minimum return loss) over all three bands and maximum S_{11} of -0.9 dB and -4.9 dB, respectively, between the lower and middle bands and middle and upper bands. In this regard, PS is superior to other reported antennas. Moreover, the three bands of the PS can be tuned independently. The low-cost compact structure is simple to design.

5. CONCLUSION

A slotted elliptical monopole is sliced from the top, and a T-strip is added to create two symmetrical loops. A slot in each loop at a different position causes the antenna to operate over the tri-bands. A rectangular stub is added to the feed line to improve impedance matching and band-stop characteristics. These three bands can be independently tuned. The antenna operates over 3.22–3.64 GHz, 5.53–6.03 GHz, and 6.71–7.14 GHz bands. This novel compact low-cost antenna is easy to fabricate and design. The antenna exhibits nearly omnidirectional radiation characteristics. The gain variation is less than 1.5 dB. Therefore, the proposed antenna is suitable for 5G, WLAN, V2X, and Wi-Fi 6E applications.

REFERENCES

[1] Kumar, G. and K. P. Ray, *Broadband Microstrip Antennas*, Artech House, 2003.

[2] Kumar, O. P., P. Kumar, T. Ali, P. Kumar, and S. Vincent, "Ultrawideband antennas: Growth and evolution," *Micromachines*, Vol. 13, No. 1, 60, 2022.

[3] Perli, B. R. and M. R. Avula, "Design of wideband elliptical ring monopole antenna using characteristic mode analysis," *Journal of Electromagnetic Engineering and Science*, Vol. 21, No. 4, 299–306, 2021.

[4] Xiang, Z., Z. Wang, C. Li, and R. You, "Design of UWB monopole antenna with ring structure based on characteristic mode theory," *Progress In Electromagnetics Research C*, Vol. 158, 225–234, 2025.

[5] Maity, B. and S. K. Nayak, "A super wideband cpw-fed elliptical slot monopole antenna for wireless applications," *Progress In Electromagnetics Research C*, Vol. 130, 139–154, 2023.

[6] Sivanagaraju, N. and M. S. S. Ram, "Design and analysis of wideband circularly polarized antenna loaded with ring structure," *Progress In Electromagnetics Research C*, Vol. 158, 57–61, 2025.

[7] Kumar, O. P., T. Ali, P. Kumar, P. Kumar, and J. Anguera, "An elliptical-shaped dual-band UWB notch antenna for wireless applications," *Applied Sciences*, Vol. 13, No. 3, 1310, 2023.

[8] Du, Y. and M. Liu, "A dual-notched ultra-wideband monopole antenna based on frequency selective surface technology," *Progress In Electromagnetics Research C*, Vol. 145, 101–105, 2024.

[9] Koohestani, M., N. Azadi-Tinat, and A. K. Skrivervik, "Compact slit-loaded ACS-fed monopole antenna for Bluetooth and UWB systems with WLAN band-stop capability," *IEEE Access*, Vol. 11, 7540–7550, 2023.

[10] Jadhav, J. B. and P. J. Deore, "Filtering antenna with radiation and filtering functions for wireless applications," *Journal of Electrical Systems and Information Technology*, Vol. 4, No. 1, 125–134, 2017.

[11] Mao, C. X., Y. Zhang, X. Y. Zhang, P. Xiao, Y. Wang, and S. Gao, "Filtering antennas: Design methods and recent developments," *IEEE Microwave Magazine*, Vol. 22, No. 11, 52–63, 2021.

[12] Jadhav, J. B. and P. J. Deore, "A compact planar ultra-wideband bandpass filter with multiple resonant and defected ground structure," *AEU — International Journal of Electronics and Communications*, Vol. 81, 31–36, 2017.

[13] Barigidad, S., A. C. Yeshawant, S. Rao, C. A. Tharunya, T. Ali, and S. Pathan, "A triple band modified F-shaped monopole antenna for RFID application," *Bulletin of Electrical Engineering and Informatics*, Vol. 9, No. 6, 2469–2476, 2020.

[14] Woo, D. S., "A triple band C-shape monopole antenna for vehicle communication application," *Progress In Electromagnetics Research C*, Vol. 121, 97–106, 2022.

[15] El Hadri, D., A. Zugari, A. Zakriti, M. E. Ouahabi, and M. Taouzari, "A compact triple band antenna for military satellite communication, radar and fifth generation applications," *Advanced Electromagnetics*, Vol. 9, No. 3, 66–73, 2020.

[16] Thiruvenkadam, S. and E. Parthasarathy, "Compact multiband monopole antenna design for IoT applications," *Journal of Electromagnetic Waves and Applications*, Vol. 37, No. 5, 629–643, 2023.

[17] Song, W., Z. Weng, Y.-C. Jiao, L. Wang, and H.-W. Yu, "Omnidirectional WLAN antenna with common-mode current suppression," *IEEE Transactions on Antennas and Propagation*, Vol. 69, No. 9, 5980–5985, 2021.

[18] Salim, A. J., J. K. Mohammed, H. Al-Saedi, and J. K. Ali, "A proximity-fed multi-band printed antenna for wireless communication applications," *Progress In Electromagnetics Research C*, Vol. 145, 153–165, 2024.

[19] Jing, J., J. Pang, H. Lin, Z. Qiu, and C.-J. Liu, "A multiband compact low-profile planar antenna based on multiple resonant stubs," *Progress In Electromagnetics Research Letters*, Vol. 94, 1–7, 2020.

[20] Verulkar, S., A. Khade, M. Trimukhe, and R. K. Gupta, "Dual band split ring monopole antenna structures for 5G and WLAN applications," *Progress In Electromagnetics Research C*, Vol. 122, 17–30, 2022.

[21] Luo, Z., T. Su, and K.-D. Xu, "A single-layer low-profile dual-wideband monopolar patch antenna with shorting vias and parasitic annular sectors," *IEEE Antennas and Wireless Propagation Letters*, Vol. 22, No. 2, 432–436, 2023.

[22] Saeed, M. J., M. M. Tahseen, and A. A. Kishk, "Compact multiband omnidirectional antenna for maximizing frequency coverage," *IEEE Antennas and Wireless Propagation Letters*, Vol. 24, No. 3, 597–601, 2025.

[23] Bharadwaj, S. S., D. Sipal, D. Yadav, and S. K. Koul, "A compact tri-band frequency reconfigurable antenna for LTE/Wi-Fi/ITS applications," *Progress In Electromagnetics Research M*, Vol. 91, 59–67, 2020.

[24] Singh, P. P., P. K. Goswami, S. K. Sharma, and G. Goswami, "Frequency reconfigurable multiband antenna for IoT applications in WLAN, Wi-Max, and C-band," *Progress In Electromagnetics Research C*, Vol. 102, 149–162, 2020.

[25] Wang, L., J. Yu, T. Xie, and K. Bi, "A novel multiband fractal antenna for wireless application," *International Journal of Antennas and Propagation*, Vol. 2021, No. 1, 9926753, 2021.

[26] Kaur, A. and P. K. Malik, "Multiband elliptical patch fractal and defected ground structures microstrip patch antenna for wireless applications," *Progress In Electromagnetics Research B*, Vol. 91, 157–173, 2021.

[27] Parasher, R., D. Yadav, and A. Saharia, "Metamaterial-based octagonal ring penta-band antenna for sub-6 GHz 5G, WLAN, and WiMAX sireless applications," *Progress In Electromagnetics Research B*, Vol. 104, 109–129, 2024.

[28] Christydass, S. P. J. and N. Gunavathi, "Dual-band complementary split-ring resonator engraved rectangular monopole for GSM and WLAN/WiMAX/5G sub-6 GHz band (new radio band)," *Progress In Electromagnetics Research C*, Vol. 113, 251–263, 2021.

[29] Asif, M., D. A. Sehrai, S. H. Kiani, J. Khan, M. Abdullah, M. Ibrar, M. Alibakhshikenari, F. Falcone, and E. Limiti, "Design of a dual band SNG metamaterial based antenna for LTE 46/WLAN and Ka-band applications," *IEEE Access*, Vol. 9, 71 553–71 562, 2021.

[30] Ray, K. P., "Design aspects of printed monopole antennas for ultra-wide band applications," *International Journal of Antennas and Propagation*, Vol. 2008, No. 1, 713858, 2008.

[31] Abdulzahra, D. H., F. Alnahwi, A. S. Abdullah, Y. I. A. Al-Yasir, and R. A. Abd-Alhameed, "A miniaturized triple-band antenna based on square split ring for IoT applications," *Electronics*, Vol. 11, No. 18, 2818, 2022.